

Finite Cell Method: High-Order Structural Dynamics for Complex Geometries

M. Elhaddad^{*,‡}, N. Zander^{*,§}, S. Kollmannsberger^{*,¶}, A. Shadavakhsh^{†,||},
V. Nübel^{†,**} and E. Rank^{*,††}

**Chair for Computation in Engineering
Technische Universität München
Arcisstr. 21, München 80333, Germany*

*†Hilti Entwicklungsgesellschaft mbH
Hiltistr. 6, Kaufering 86916, Germany*

‡mohamed.elhaddad@tum.de

§nils.zander@tum.de

¶stefan.kollmannsberger@tum.de

||ermst.rank@tum.de

***ali.shadavakhsh@hilti.com*

††vera.nuebel@hilti.com

Received 12 December 2014

Accepted 16 February 2015

Published 13 April 2015

In this contribution, the finite cell method (FCM) is applied to solve transient problems of linear elastodynamics. The mathematical formulation of FCM for linear elastodynamics is presented, following from the weak formulation of the initial/boundary-value problem. Semi-discrete time integration schemes are briefly discussed, and the choice of implicit time integration is justified. A 1D benchmark problem is solved using FCM, illustrating the method's ability to solve problems of linear elastodynamics obtaining high rates of convergence. Furthermore, a numerical example of transient analysis from an industrial application is solved using FCM. The numerical results are compared to the results obtained using state-of-the-art commercial software, employing linear finite elements, in conjunction with explicit time integration. The results illustrate the potential of FCM as a powerful tool for transient analysis in elastodynamics, offering a high degree of accuracy at a moderate computational effort.

Keywords: Finite cell method; implicit dynamics.

1. Introduction

Time-dependent problems of elastodynamics are of great importance in engineering practice. As fatigue accounts for nearly 90% of all mechanical failures,¹ an adequate treatment of transient loads is necessary to ensure a reliable design. Numerical methods are employed to gain insight into the dynamic behavior of mechanical

systems. The finite element method (FEM) is extensively used for the solution of initial/boundary-value problems in several engineering disciplines.^{2,3} Conventional finite element analysis requires the spatial discretization of the physical domain using geometry conforming finite elements. Complex geometries, which are common in engineering practice, require meshing procedures which can be quite time consuming. In fact, up to 80% of the overall analysis time can be attributed to the generation of a mesh suitable for finite element analysis.⁴

A fine spatial discretization is needed in order to resolve fine geometric details. This yields large systems of equations, making explicit time integration the more feasible choice. However, explicit schemes require small critical time steps for fine spatial discretizations to maintain numerical stability. For some applications (e.g. wave propagation), such time steps are appropriate. However, for applications in structural dynamics, fine discretizations lead to unduly small time steps,² making long time spans of observation a challenge. Furthermore, in state-of-the-art explicit dynamics software such as LS-DYNA, under-integration is widely used for numerical efficiency and to counteract shear and volumetric locking.⁵ However, under-integration causes some side-effects for which no complete satisfactory solutions have been found. Most prominently, under-integration may result in rank deficiency of the discrete system, causing instabilities in the form of “hourglass modes”.^{2,3}

The finite cell method (FCM) is an immersed boundary method based on high order finite elements.⁶ The main idea is to extend the physical domain by a slightly larger embedding domain of simple geometry which can be easily meshed. FCM avoids the geometric complexity on the mesh level, thereby circumventing the time consuming meshing procedures. Instead, the geometric information is taken into account on the integration level by penalizing integration points that are outside the physical domain, thereby recovering the original problem. Using adaptive integration techniques, FCM retains the high convergence rates of the underlying high order finite elements for smooth problems.⁶⁻⁸

The FCM has been investigated for problems of solid mechanics on complex Computer-aided-design (CAD)-based geometries,⁹ for linear and geometrically nonlinear behavior.¹⁰ The potential of FCM as a seamless geometry-through-analysis procedure was demonstrated, opening the door for further applications. Recent publications confirm the method’s applicability in the context of elastoplasticity,¹¹ treatment of shell-like structures,¹² biomechanical applications,¹³ local enrichment for material interfaces¹⁴ and adaptive mesh refinement.^{8,15} An extension of FCM with mass lumping techniques in conjunction with explicit time integration has been proposed by Joulaian *et al.*,¹⁶ and applied successfully for the analysis of wave propagation in heterogeneous materials.

In this contribution, FCM is employed to solve time-dependent problems of linear elastodynamics. Avoiding the restriction of having a geometry conforming mesh, complex geometries are easily handled. Furthermore, the method reaps the benefits of its high order p -version approximation basis, namely the high convergence rates

and locking-free behavior. Hence, for the same degree of accuracy, the FCM discretization results in systems that are relatively small in terms of degrees of freedom. Such systems can be efficiently solved using implicit time integration schemes, allowing for much larger time steps, compared to explicit schemes.

The present work is organized as follows: Section 2 presents the mathematical formulation of the finite cell method for linear elastodynamics. Starting from the weak form of the initial/boundary-value problem, the spatial discretization leads to the semi-discrete Galerkin formulation. An extension of the solution over an embedding domain leads to the weak formulation for the finite cell method. In Sec. 3, the ability of FCM to solve problems of linear elastodynamics with high convergence rates is illustrated with a simple benchmark problem. A second example involving a complex 3D geometry is solved with FCM, demonstrating the feasibility of using FCM for industrial problems. Finally, Sec. 4 closes with some concluding remarks and suggests several possibilities for further development.

2. The Finite Cell Method for Linear Elastodynamics

In this section, the mathematical formulation of the FCM for linear elastodynamics is briefly introduced.

2.1. Weak form

Consider an elastic continuum, which is described by the physical domain Ω_{phy} . The physical domain's boundary comprises a Dirichlet and a Neumann part $\partial\Omega_{\text{phy}} = \Gamma_D \cup \Gamma_N$, which are nonintersecting $\Gamma_D \cap \Gamma_N = \emptyset$. The weak form of the initial/boundary value problem of linear elastodynamics reads³:

Find $\mathbf{u}(\mathbf{x}, t) \in \mathcal{S}^t(\Omega_{\text{phy}})$, $t \in [t_0, T]$ such that:

$$\mathcal{D}(\dot{\mathbf{u}}, \mathbf{v}) + \mathcal{C}(\dot{\mathbf{u}}, \mathbf{v}) + \mathcal{B}(\mathbf{u}, \mathbf{v}) = \mathcal{F}(\mathbf{v}) \quad \forall \mathbf{v} \in \mathcal{V}(\Omega_{\text{phy}}), \quad (1a)$$

with the initial conditions:

$$\mathcal{D}(\mathbf{u}(t_0), \mathbf{v}) = \mathcal{D}(\hat{\mathbf{u}}_0, \mathbf{v}) \quad \text{and} \quad \mathcal{C}(\dot{\mathbf{u}}(t_0), \mathbf{v}) = \mathcal{C}(\hat{\dot{\mathbf{u}}}_0, \mathbf{v}), \quad (1b)$$

where

$$\begin{aligned} \mathcal{D}(\dot{\mathbf{u}}, \mathbf{v}) &= \int_{\Omega_{\text{phy}}} \rho \dot{\mathbf{u}} \cdot \mathbf{v} \, d\Omega, & \mathcal{C}(\dot{\mathbf{u}}, \mathbf{v}) &= \int_{\Omega_{\text{phy}}} \dot{\mathbf{u}} \cdot \boldsymbol{\kappa} \cdot \mathbf{v} \, d\Omega, \\ \mathcal{B}(\mathbf{u}, \mathbf{v}) &= \int_{\Omega_{\text{phy}}} \nabla \mathbf{v} : \mathbb{C} : \nabla \mathbf{u} \, d\Omega, & \mathcal{F}(\mathbf{v}) &= \int_{\Omega_{\text{phy}}} \mathbf{b} \cdot \mathbf{v} \, d\Omega + \int_{\Gamma_N} \hat{\mathbf{t}} \cdot \mathbf{v} \, d\Gamma, \end{aligned}$$

in which ρ , $\boldsymbol{\kappa}$, \mathbb{C} , \mathbf{u} , $\dot{\mathbf{u}}$, $\ddot{\mathbf{u}}$ and \mathbf{v} denote the density, the matrix of viscous damping coefficients, the elasticity tensor, the displacement, velocity and acceleration vectors, and the test functions, respectively. \mathbf{b} and $\hat{\mathbf{t}}$ denote the body load and the surface traction applied on the Neumann boundary, respectively. \mathcal{S}^t is the trial solution space, which is constructed such that \mathbf{u} satisfies the Dirichlet (essential) boundary

conditions

$$\mathcal{S}^t(\Omega_{\text{phy}}) = \{\mathbf{u} \mid \mathbf{u} \in H^1(\Omega_{\text{phy}}), \mathbf{u} = \hat{\mathbf{u}} \forall (\mathbf{x}, t) \in \Gamma_D \times]t_0, T[\}, \quad (2)$$

whereas $\mathcal{V}(\Omega_{\text{phy}})$ denotes the space of all admissible test functions, which satisfy the homogeneous Dirichlet boundary condition

$$\mathcal{V}(\Omega_{\text{phy}}) = \{\mathbf{v} \mid \mathbf{v} \in H^1(\Omega_{\text{phy}}), \mathbf{v} = \mathbf{0} \forall \mathbf{x} \in \Gamma_D \}. \quad (3)$$

H^1 denotes the Sobolev space¹⁷ of first order. The bilinear form $\mathcal{D}(\hat{\mathbf{u}}, \mathbf{v})$ defines the virtual work done by the inertia forces, for a virtual displacement \mathbf{v} . Similarly, $\mathcal{C}(\hat{\mathbf{u}}, \mathbf{v})$ and $\mathcal{B}(\mathbf{u}, \mathbf{v})$ describe the energy dissipated by the damping forces, and the virtual work done by the internal stresses, respectively. The linear functional $\mathcal{F}(\mathbf{v})$ represents the virtual work done by the external forces. The weak form of the initial conditions, described by Eq. (1b) corresponds to an L_2 projection of the initial conditions $\mathbf{u}(t_0) = \hat{\mathbf{u}}_0$ and $\dot{\mathbf{u}}(t_0) = \hat{\mathbf{u}}_0$ onto the variation space \mathcal{V} .

2.2. Spatial discretization of the weak form

The principal idea of the finite element method is to approximate the solution of the weak form by a discrete solution $\mathbf{u}_h \in \mathcal{S}_h^t$, and a corresponding discrete test function $\mathbf{v}_h \in \mathcal{V}_h$. The finite dimensional subspaces $\mathcal{S}_h^t \subset \mathcal{S}^t$ and $\mathcal{V}_h \subset \mathcal{V}$ are associated with a mesh, or a spatial discretization of the physical domain Ω_{phy} . The approximate solution \mathbf{u}_h is still temporally continuous, hence the name semi-discrete.

Representing \mathbf{u}_h by the basis $\{N_1, N_2, \dots, N_n\}$ spanning \mathcal{S}_h^t

$$\mathbf{u}_h(\mathbf{x}, t) = \sum_{i=1}^n N_i(\mathbf{x}) \mathbf{d}_i(t), \quad (4)$$

and following the standard Bubnov–Galerkin approach, the test functions \mathbf{v} are represented by the same basis,³ leading to a system of linear equations. The matrix form of the initial/boundary-value problem for linear elastodynamics is then expressed as:

Find $\mathbf{d}(t), t \in [t_0, T]$ such that:

$$\mathbf{M}\ddot{\mathbf{d}}(t) + \mathbf{C}\dot{\mathbf{d}}(t) + \mathbf{K}\mathbf{d}(t) = \mathbf{f}(t), \quad (5a)$$

$$\text{with } \mathbf{d}(t_0) = \hat{\mathbf{d}}_0 \quad \text{and} \quad \dot{\mathbf{d}}(t_0) = \hat{\mathbf{d}}_0, \quad (5b)$$

where \mathbf{M} is the mass matrix, \mathbf{C} the damping matrix, \mathbf{K} the stiffness matrix and \mathbf{f} the load vector.

2.3. Concept of the finite cell method

The physical domain Ω_{phy} is augmented by a fictitious domain Ω_{fict} to form the extended domain Ω_{\cup} , as illustrated by Fig. 1. The extended domain has a simple shape that is easily meshed, thereby evading the geometric complexity of Ω_{phy} on the mesh level.^{6,7}

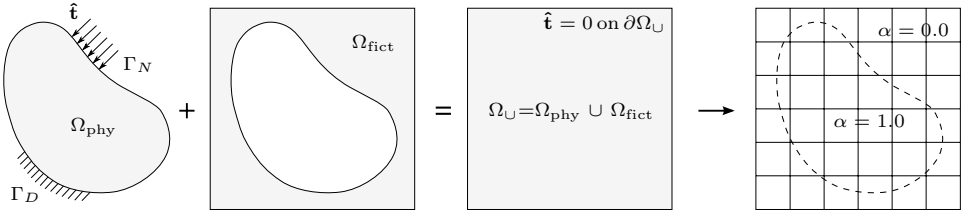


Fig. 1. Concept of the finite cell method, taken from Ref. 10.

The weak formulation is modified by defining the weak form integrals over the extended domain Ω_U . Additionally, the virtual work terms are multiplied by a scalar field $\alpha(\mathbf{x})$:

$$\begin{aligned} \mathcal{D}_e(\ddot{\mathbf{u}}, \mathbf{v}) &= \int_{\Omega_U} \alpha \rho \ddot{\mathbf{u}} \cdot \mathbf{v} \, d\Omega, & \mathcal{C}_e(\dot{\mathbf{u}}, \mathbf{v}) &= \int_{\Omega_U} \dot{\mathbf{u}} \cdot \alpha \boldsymbol{\kappa} \cdot \mathbf{v} \, d\Omega, \\ \mathcal{B}_e(\mathbf{u}, \mathbf{v}) &= \int_{\Omega_U} \nabla \mathbf{v} : \alpha \mathbb{C} : \nabla \mathbf{u} \, d\Omega, & \mathcal{F}_e(\mathbf{v}) &= \int_{\Omega_U} \alpha \mathbf{b} \cdot \mathbf{v} \, d\Omega + \int_{\Gamma_N} \hat{\mathbf{t}} \cdot \mathbf{v} \, d\Gamma, \end{aligned}$$

with α defined such that:

$$\alpha(\mathbf{x}) = \begin{cases} 1 & \forall \mathbf{x} \in \Omega_{\text{phy}} \\ 10^{-q} & \forall \mathbf{x} \in \Omega_{\text{fict}}. \end{cases}$$

The influence of the fictitious domain is mitigated by assigning a very small value to α in Ω_{fict} . Physically, this can be interpreted as a scaling of the material parameters, ρ , $\boldsymbol{\kappa}$ and \mathbb{C} , thereby filling the fictitious domain with a “void material” which is very compliant, lightweight and undamped. Practically, α_{fict} should be assigned a value as small as possible, but large enough to prevent extreme ill-conditioning of the system matrices. Typical values range between 10^{-4} and 10^{-15} .

The extended domain is discretized using a Cartesian grid of high order finite elements. Several possibilities exist for the choice of Ansatz functions. The integrated Legendre polynomials, used in the p -version of FEM, and B-Splines are suitable basis for FCM, when mass lumping is not required.¹⁰ Alternatively, Lagrange polynomials based on Gauss–Lobatto quadrature have been successfully applied to FCM, together with mass lumping schemes leading to the spectral cell method.¹⁶ In the present work, we use the p -version of FCM, as we apply implicit time integration. Standard Gaussian quadrature is not suitable for the numerical integration of the finite cells which are cut by the boundary, as the integrands are discontinuous. Several possibilities exist for numerical integration of cut cells in the framework of the finite cell method. An investigation of different schemes in the context of FCM is presented in Ref. 18.

One approach is to adaptively partition the cut-cells using an octree structure in 3D (binary tree in 1D, quadtree in 2D). A standard Gaussian quadrature is then applied per sub-cell (leaf node). This approach is easy to implement and can be used for the fully automatic generation of the integration sub-cells, retaining the

convergence rates of FCM when the tree is sufficiently refined. Moreover, this approach does not require an explicit description of the boundary, as only an inside–outside test is performed.^{6,7} This makes it more versatile and applicable to both CAD-based and voxel-based geometry description.⁸

2.4. Temporal discretization

The spatial discretization of the weak form of the initial/boundary-value problem leads to a system of coupled, second-order, ordinary differential equations. Several methods are available in the literature for their solution; see Refs. 2 and 3. Finite difference schemes are commonly used for the temporal discretization, based on either explicit or implicit formulations. In the present work, the implicit Newmark- β scheme^{2,3} is employed for temporal discretization, in conjunction with the finite cell method for spatial discretization to solve time-dependent problems of linear elastodynamics. The implicit stepping scheme requires the solution of a system of linear equations at each time step. However, a much smaller number of steps are needed, in comparison with an explicit scheme, for the resolution in the time domain with sufficient accuracy. This allows for longer observation times, which are practically impossible with explicit schemes.

3. Numerical Examples

In this section, we present numerical examples of linear elastodynamics solved using the FCM.

3.1. Uniaxial bar benchmark

The following 1D benchmark illustrates the basic properties of the numerical solution obtained using the finite cell method for problems of linear elastodynamics.

3.1.1. Analysis setup

We consider a uniaxial bar, which is clamped at one end (fixed-free), and subjected to a traction at the other end, as depicted in Fig. 2. We assume the bar is rigid with

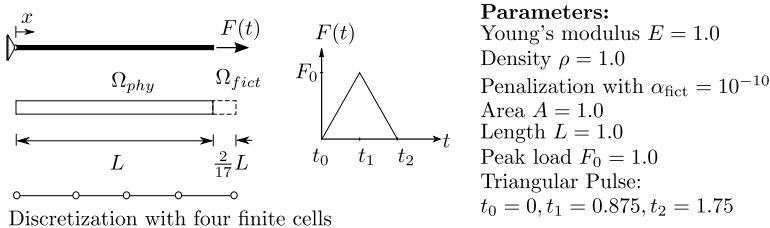


Fig. 2. Setup of the uniaxial bar benchmark.

respect to bending (bending stiffness $EI \rightarrow \infty$) and only the longitudinal deformation $u(x, t)$ is considered. The time-dependent load $F(t)$ is a triangular impulse, with a duration $t_2 = 1.75$. The total time span of observation is $T = 14$.

3.1.2. Numerical results

The bar is embedded in an extended domain of total length $\frac{19}{17}L$ as illustrated in Fig. 2. The domain is uniformly discretized using four finite cells. Note that for this discretization, the end of the physical bar does *not* coincide with any node of this 1D mesh of finite cells. The Neumann boundary condition is therefore applied in the *interior* of the rightmost cell. For numerical integration, a binary tree of depth $k = 20$ is used to partition the cut element as described in Sec. 2.3, using $p + 1$ quadrature points per sub-cell, where p is the polynomial degree. $\alpha_{\text{fict}} = 10^{-10}$ is used to penalize the influence of the fictitious domain. To study the convergence properties, a p -extension is carried out with $p = 1, 2, \dots, 25$. An h -extension with 8, 16, 32, 64 and 128 elements is also carried out for comparison.

The Newmark- β scheme is employed for time integration, with $\gamma = \frac{1}{2}$ and $\beta = \frac{1}{4}$. Since we investigate the accuracy of the spatial discretization, the time step size is chosen small enough, such that the spatial discretization error dominates the total error. Here, we use 36,480 time steps for the whole time span. A reference solution is computed using modal analysis and the Duhamel integral.¹⁹

Figure 3 depicts the excellent approximation of the transient displacement at the tip of the bar. Figure 4 shows the displacement at time $t = 5.875$ along the bar. By construction, the displacement field extends beyond the end of the physical domain, meaning, that formally also strains and stresses are defined in the fictitious domain.

Figure 5 depicts the strain distribution in logarithmic scale. Whereas in the physical domain, FCM results match the analytic reference solution very well, the

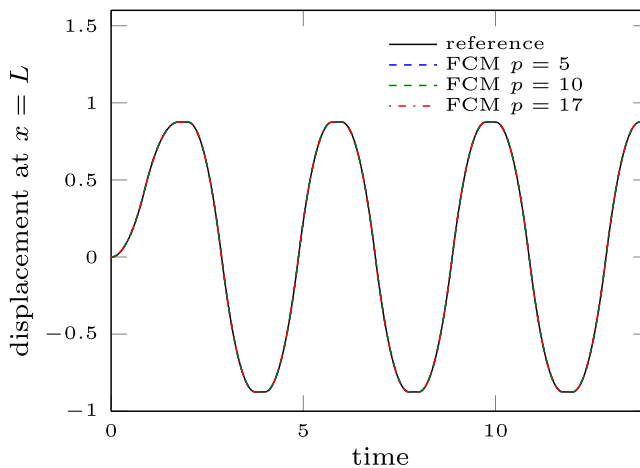


Fig. 3. Displacement at $x = L$.

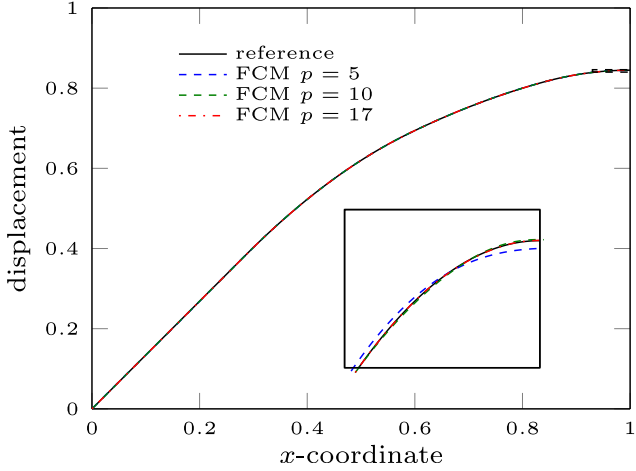


Fig. 4. Displacement at $t = 5.875$.

oscillatory behavior in the fictitious part is out of the domain of interest and can be neglected.

Figure 6 looks closer to the approximation of strains in the interior of the bar. The triangular impulse traction propagates through the bar as an elastodynamic wave, which is reflected at the boundaries. The analytical strain field is piecewise linear, exhibiting three kinks corresponding to the kinks in the load function propagating along the bar. As the numerical approximation is only a C^0 -continuous function of piecewise polynomials, it cannot represent the solution exactly. Slight oscillations can be seen in the vicinity of the kinks in the strain, as shown in Fig. 6. Yet, they quickly decrease with increasing polynomial order of the shape functions.

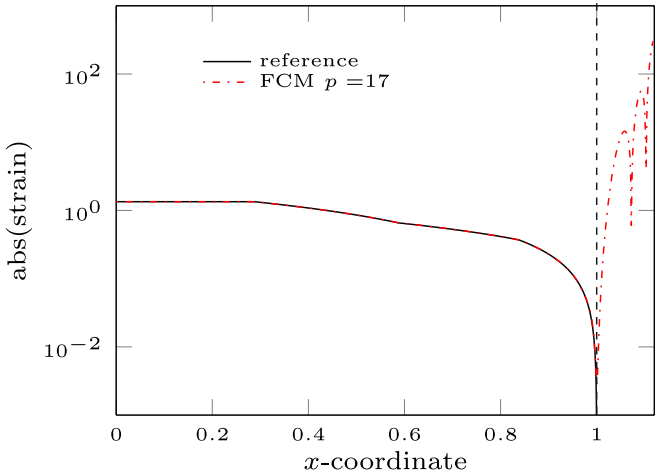
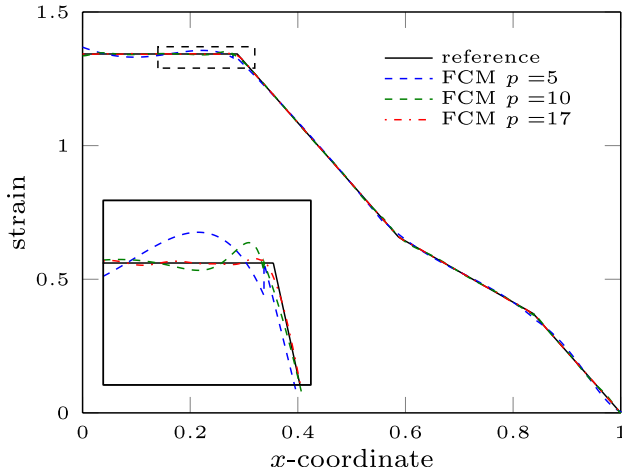


Fig. 5. Strain at $t = 5.875$ in logarithmic scale.


 Fig. 6. Strain at $t = 5.875$ in linear scale.

To study the convergence in the energy norm, the error measure

$$\eta(t) = \sqrt{\frac{|\Delta E_{\text{str}}(t)| + |\Delta E_{\text{kin}}(t)|}{E_{\text{max}}}} \quad (6)$$

is introduced, where $\Delta E_{\text{str}}(t)$ and $\Delta E_{\text{kin}}(t)$ denote the error in strain and kinetic energy, respectively. Figure 7 displays the maximum error $\eta_{\text{max}} = \max_t \eta(t)$. As shown in the figure, the finite cell method with both h - and p -extensions converge algebraically, with the p -extension having a higher rate. This is explained by the smoothness of the solution, as the exact solution is not an *analytic* function (not

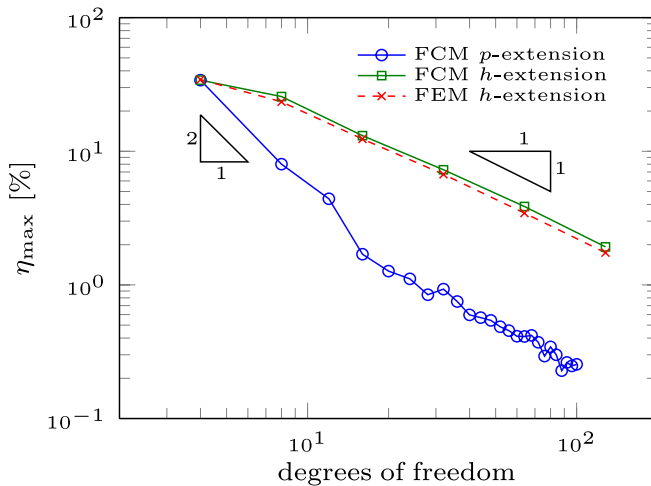


Fig. 7. Convergence for the uniaxial bar with transient load.

representable by a Taylor series expansion).²⁰ Hence, both h - and p -extension converge algebraically, with the p -extension having a higher rate. This allows the p -extension, with a discretization of about 20 degrees of freedom, to obtain an error which is one order of magnitude lower than that of the h -extension. It is also observed that the embedded domain approach does not introduce any significant loss in accuracy, when compared to a geometry conforming FEM discretization.

3.2. Industrial example

In this example, the subject of the transient analysis is the chuck of a hammer-action drill, which transmits the impact force from a ram to the drill bit. This example illustrates the potential of FCM as a powerful numerical tool for the solution of time-dependent problems on CAD geometries.

3.2.1. Analysis setup

The chuck's geometry, shown in Fig. 8, is represented by a B-rep (boundary representation) CAD model, where the boundary is described by trimmed NURBS surfaces. The part resembles a hollow cylindrical shaft with three axial sections, with the diameters changing between the sections. The chuck contains two slotted holes at the front section. It is 235 mm long, has outer diameters 26.0, 30.2 and 51.4 mm at the front, rear and middle sections respectively, and a wall thickness of 4.0 mm throughout. The chuck is made of steel with Young's modulus 210 GPa, Poisson's ratio 0.3 and density 7850 kg/m³. The whole part weighs 0.75 kg. In the analysis at hand, damping is neglected. The impact load is modeled as an axially directed surface traction, which is uniformly distributed over the impact surface. The transient load function is modeled by a triangular pulse, with a peak force F_0 of 110 kN at $t_1 = 0.031$ ms and a total duration $t_2 = 0.066$ ms. The total time span of the transient analysis is 0.5 ms.

3.2.2. Discretization

The FCM is used for a non-geometry conforming spatial discretization. The numerical simulations were carried out using the in-house high order FEM code AdhoC++. As the geometry and the load are symmetric around the transverse and longitudinal planes, only one quarter of the problem is considered, and symmetry

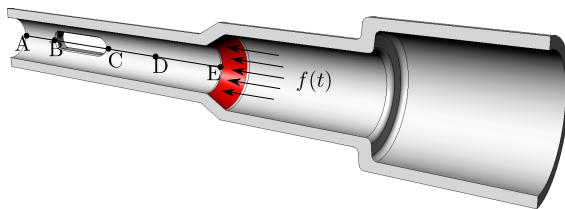


Fig. 8. Chuck analysis setup.

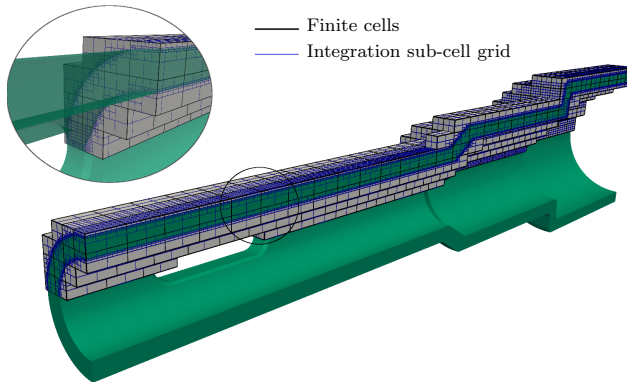


Fig. 9. Chuck example — discretization using FCM.

boundary conditions applied. The chuck’s bounding box is discretized uniformly by $8 \times 30 \times 8$ axis-aligned finite cells. The cells which lie completely outside the physical domain are excluded from the analysis, leaving 533 finite cells. A convergence study with p -extension based on the tensor product space²⁰ is carried out for an isotropic polynomial degree $p = 1, 2, \dots, 5$.

For numerical integration, the elements cut by the boundary of the chuck are adaptively partitioned using an octree of depth $k = 4$ as described in Sec. 2.3, yielding a total number of 361,474 integration sub-cells as shown in Fig. 9. Integration is carried out using a Gauss–Legendre quadrature with $(p + 1)^3$ points per sub-cell. Integration points which lie outside the physical domain are penalized by $\alpha_{\text{fict}} = 10^{-4}$.

An inside–outside test is an important component of the finite cell analysis pipeline. Several possibilities exist for CAD-based geometries. One option is the voxelization of the geometry, where a Boolean value is assigned to each point, indicating whether it lies inside or outside the structure. Alternatively, a space partitioning scheme using a k - d tree operating on an STL surface parametrization is used, which is implemented in the software library `VirtualFluids`.²¹ The STL parametrization was prepared using the CAD modeling software `RhinoCeros`,²² with 200,558 triangles describing the boundary surface. The surface traction modeling the impact is treated as a time-dependent Neumann boundary condition, which is numerically integrated over the impact surface. An STL surface parametrization is used for its description with 12,049 triangles.

Here, the Newmark- β direct time integration scheme is applied for time integration, with $\beta = \frac{1}{4}, \gamma = \frac{1}{2}$. Following the procedure described by Bathe,² the significant frequencies contained in the transient load are identified by means of Fourier analysis.¹⁹ The load’s frequency spectrum, depicted in Fig. 10, shows that the loading contains significant frequencies up to 30 kHz. By choosing $f_{\text{co}} = 30$ kHz as the cutoff frequency, a suitable time step is at least $\Delta t = (20f_{\text{co}})^{-1}$. Hence, the recommended number of time steps is at least 300. We use 400 time steps, which we expect to resolve the 0.5 ms time span with sufficient accuracy.

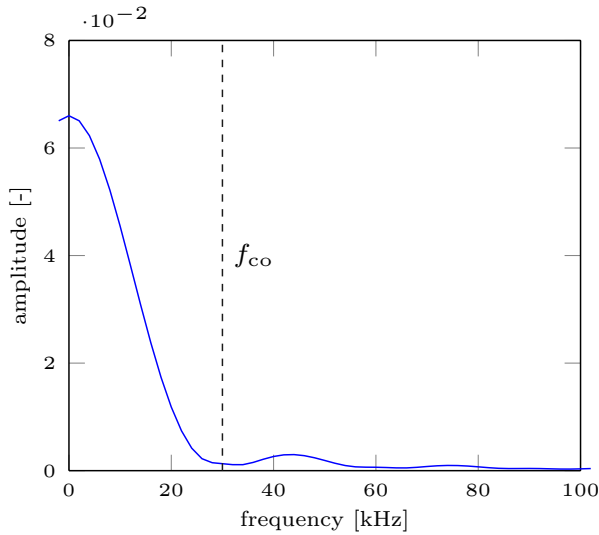


Fig. 10. Fourier transformation of the load function.



Fig. 11. Chuck example — discretization using linear tetrahedral finite elements.

For comparison, the problem is also solved with a geometry conforming discretization by linear tetrahedral finite elements using the commercial explicit finite element software LS-DYNA.⁵ The discretization, which is depicted in Fig. 11, results in a total number of 366,097 elements with 76,786 nodes, having 230,358 degrees of freedom. Note that one half of the problem is considered here, whereas only one quarter is considered for the solution using the finite cell method. The fine spatial discretization requires a critical time step of 1.07×10^{-8} s, totalling in 45,526 steps for the 0.5 ms time span, which is about 150 times more than the number of steps required for an implicit transient analysis.

3.2.3. Numerical results

In the following, the results of the p -extension are presented and compared to the results obtained using LS-DYNA. The latter are not intended as a reference solution, as the given discretization is expected to still exhibit a significant approximation error. Nevertheless, on convergence plots which have the number of degrees of freedom as their abscissæ, the results from LS-DYNA are shown for comparison as a horizontal line, and the ordinates normalized to the LS-DYNA results.

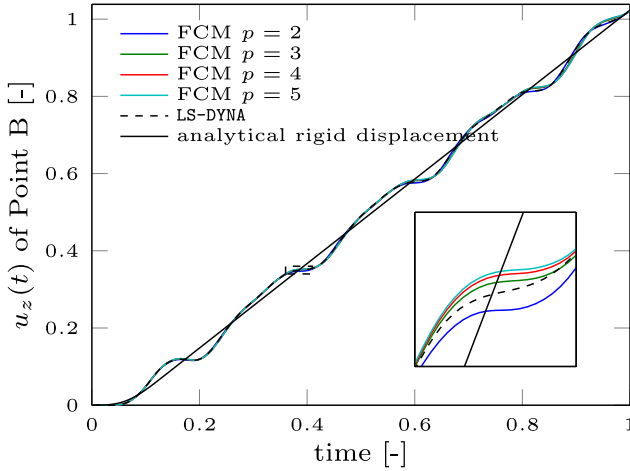


Fig. 12. Time history of axial displacement at Point B.

Figure 12 depicts the computed axial displacements at Point B. As the part is unconstrained, the axial displacements comprise a rigid body displacement and an elastic vibration. Since the load function is known explicitly, the rigid body displacement can be easily determined using the Duhamel integral.¹⁹ It can be observed in Fig. 12 that the computed axial displacements agree well with the analytical rigid body displacements. Note that the initial “silence” period is explained by the superposition of the rigid body displacements and the elastic displacement. The sum of both displacement components during the initial period balances out to zero, until the elastic wave reaches Point B from the impact surface. The convergence of the maximum elastic axial displacements at Points B, C and D is shown in Figs. 13–15.

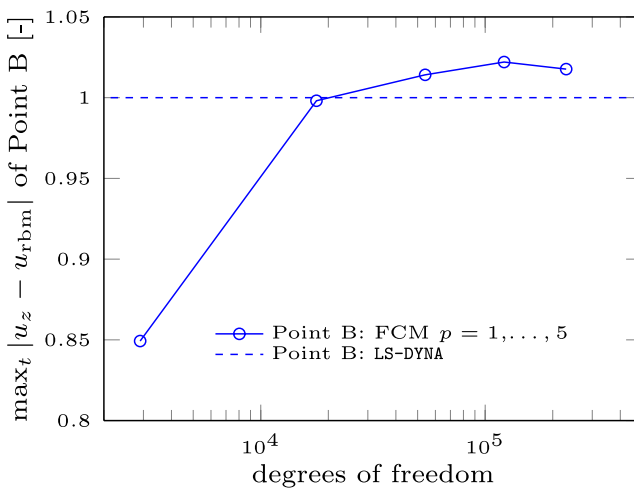


Fig. 13. Convergence of maximum elastic axial displacement at Point B.

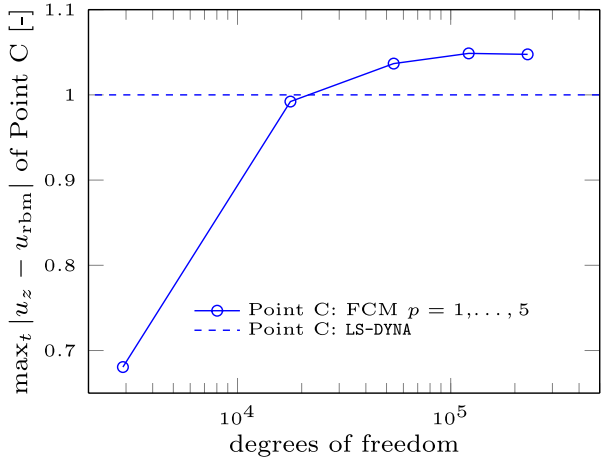


Fig. 14. Convergence of maximum elastic axial displacement at Point C.

Figure 16 shows the time history of the radial displacement at Point B. The convergence of the maximum radial displacement at Points B and C is depicted in Figs. 17 and 18. It can be seen that the converged FCM solution agrees well with the solution obtained using LS-DYNA.

The kinetic energy comprises a part associated with the rigid body motion and an elastic part. Following the loading phase, the rigid part remains constant due to a constant rigid body velocity. An undamped free vibration follows, as the elastic energy oscillates between elastic strain (potential) and elastic-kinetic energy as illustrated by Figs. 19 and 20. The parameters for the Newmark- β scheme were

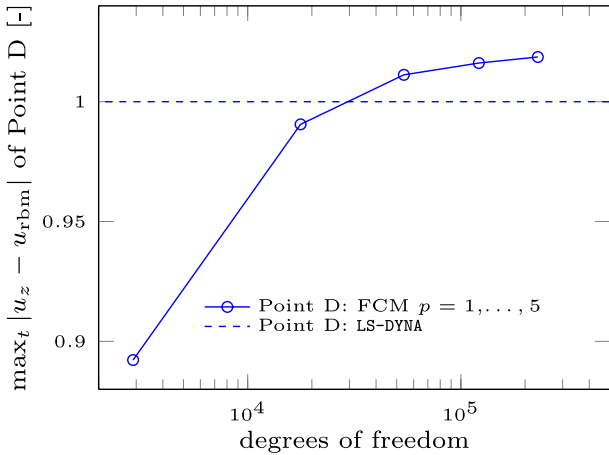


Fig. 15. Convergence of maximum elastic axial displacement at Point D.

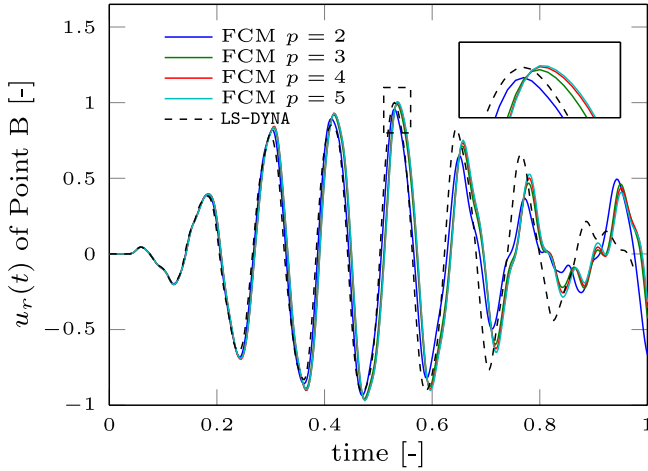


Fig. 16. Time history of radial displacement at Point B.

chosen such that no numerical damping occurs, which is evident as the total energy remains constant. The results also show that the conservation of energy is maintained, even with a nonconforming discretization using FCM. Figure 21 also demonstrates the convergence of the response frequencies from above for the p -extension. This convergence behavior is typical when using the consistent mass matrix,^{2,3} as the system becomes less stiff with increasing polynomial degree. Figure 22 demonstrates the convergence of the total energy.

The resulting stresses computed with the finite cell method show stress concentrations at the slotted hole as depicted in Fig. 23 and at the reentrant corners at the flange transition between the rear and middle sections as shown in Fig. 24.

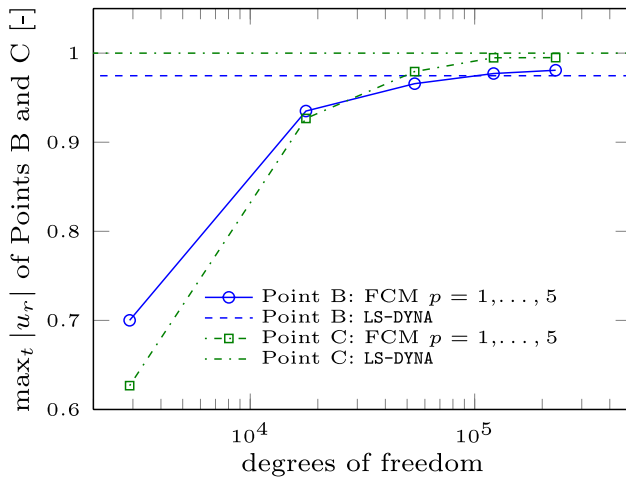


Fig. 17. Convergence of maximum radial displacement at Point B.

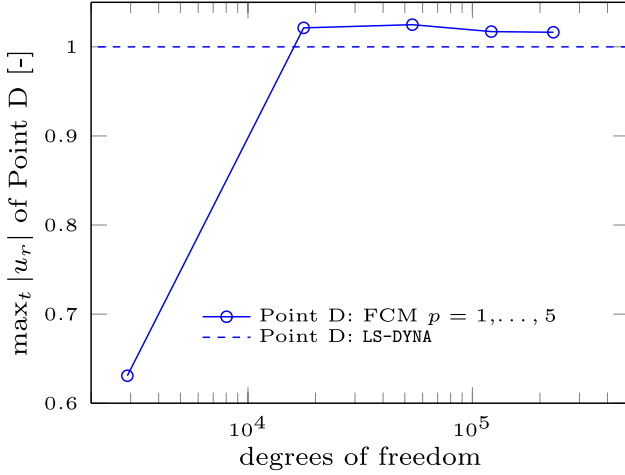


Fig. 18. Convergence of maximum radial displacement at Point D.

It is interesting to point out the distribution of the normal axial stresses over the thickness, occurring when the slotted hole expands and contracts as depicted in Fig. 25. The deformation and the stress distribution show a bending deformation, which would induce shear locking when represented by linear shape functions.^{2,3} The deformation is, however, easily represented by the high order basis functions used by FCM.^{20,23}

The stresses at Point D (away from the slotted hole) exhibit fast convergence, as evident in Figs. 26 and 27. The FCM results agree very well with the LS-DYNA computation, as observed in Fig. 27. At Points B and C, directly at the slotted hole, stresses of much higher values are computed. The stresses at these two points are

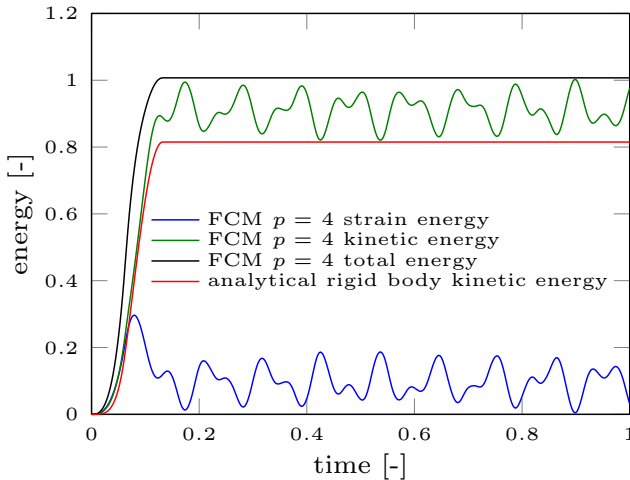


Fig. 19. Energy time history.

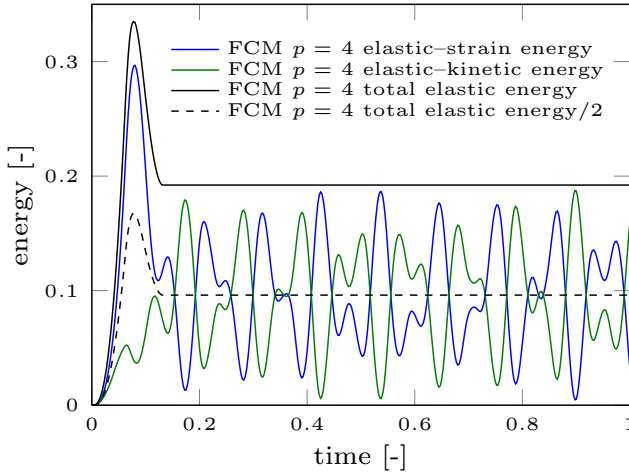


Fig. 20. Elastic energy time history.

mainly dominated by the normal tangential component which is depicted in Fig. 28. At both points, the computed maximum values for the von Mises stresses, are close to the values obtained from LS-DYNA as shown in Fig. 29.

To further investigate the convergence of the maximum stresses in the vicinity of the slotted hole, we plot the von Mises stresses along line A–E at the instant when the maximum stresses occur. The stress plots (Figs. 30(a) and 30(b)) show very high stress gradients in the vicinity of the hole. A closer look reveals that the jumps in the stresses across element boundaries diminish with increasing p , indicating a decreasing error. However, due to the local nature of the problem, convergence is slow under uniform p -extension. For this problem, local mesh refinement is necessary to ensure

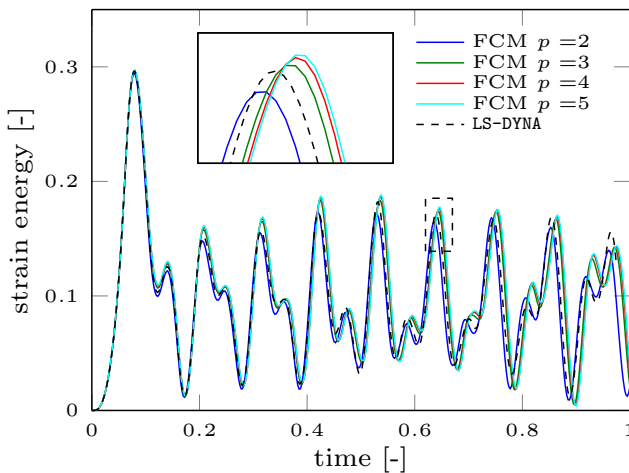


Fig. 21. Strain energy time history.

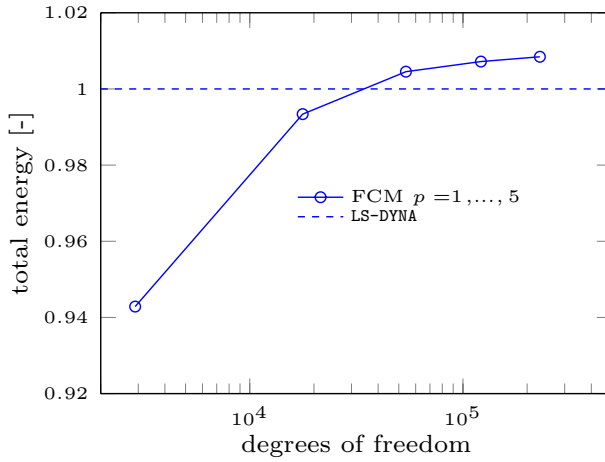


Fig. 22. Convergence of total energy.

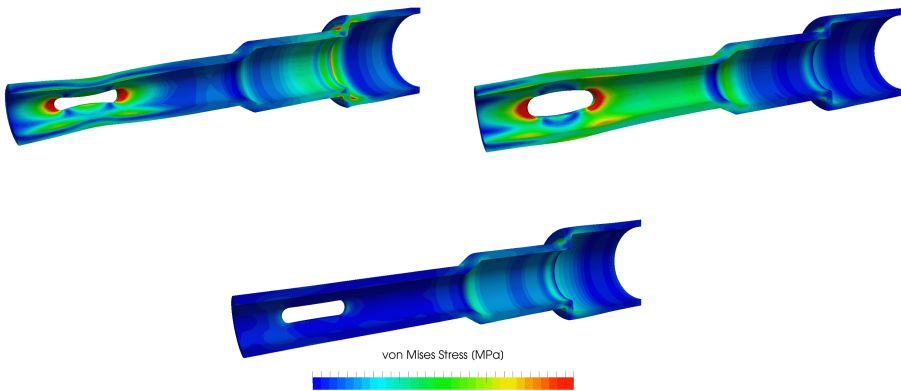


Fig. 23. Von Mises Stress shown on the deformed configuration (scaling factor = 60, obtained using FCM with $p = 4$).

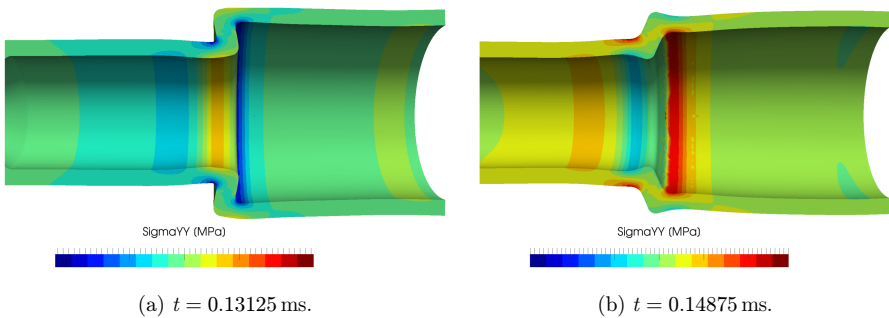


Fig. 24. Normal stresses shown on the deformed configuration, obtained using FCM with $p = 4$. Displacements scaled by a factor 100.

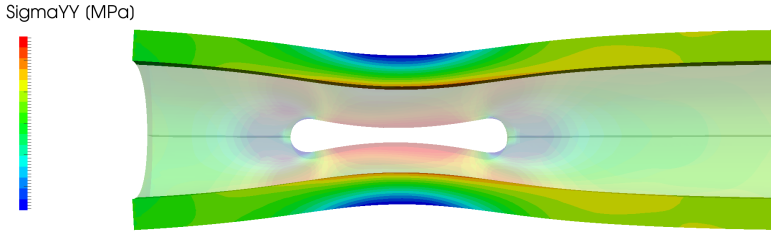


Fig. 25. Normal axial stress distribution through the thickness at $t = 0.14375$ ms. Displacements scaled by a factor 100.

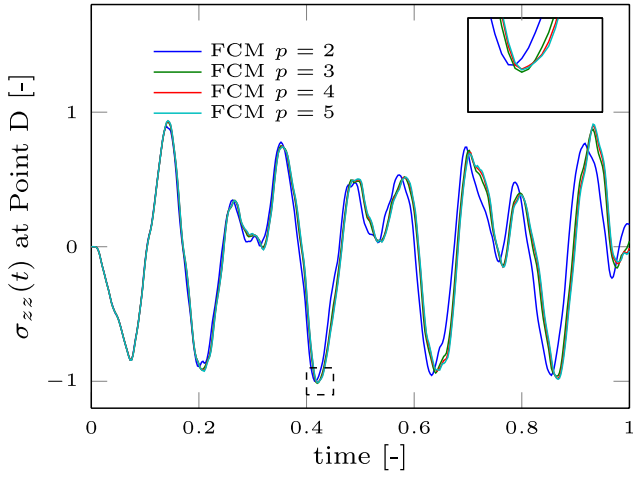


Fig. 26. Time history of normal axial stresses at Point D.

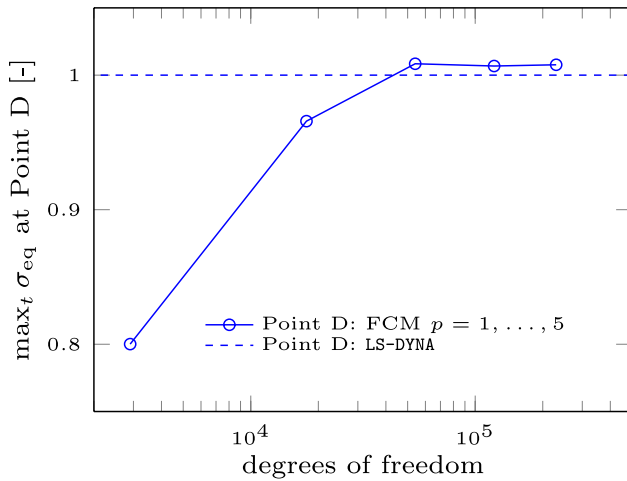


Fig. 27. Convergence of maximum von Mises stress at Point D.

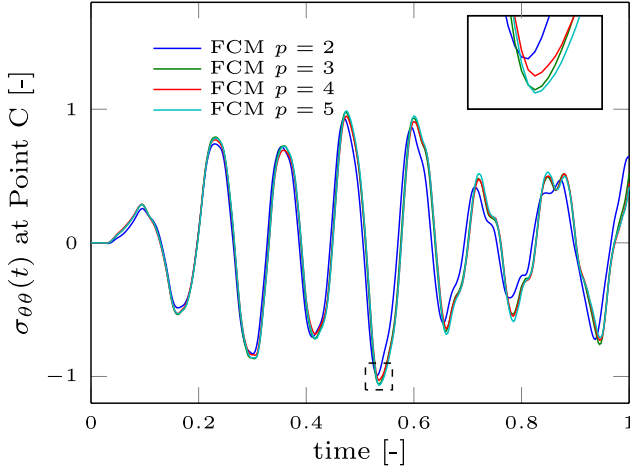


Fig. 28. Time history of normal tangential stresses at C.

an accurate numerical solution. In the context of FCM, this can be achieved by applying hierarchical hp - d adaptivity, as demonstrated in Refs. 8 and 15.

Summarizing the findings, we conclude that both simulations, FCM and classical explicit finite elements obtained by LS-DYNA, yield very similar results, despite the different spatial and time discretization schemes being used. Global assessment of the solution shows convergence of the total energy or the finite cell analysis with uniform p -extension. The frequencies of the response also converge from above, which is expected when using the consistent mass matrix.

In comparison, the response obtained using from LS-DYNA can be described as being stiffer, as suggested by the slightly higher response frequencies, and the lower

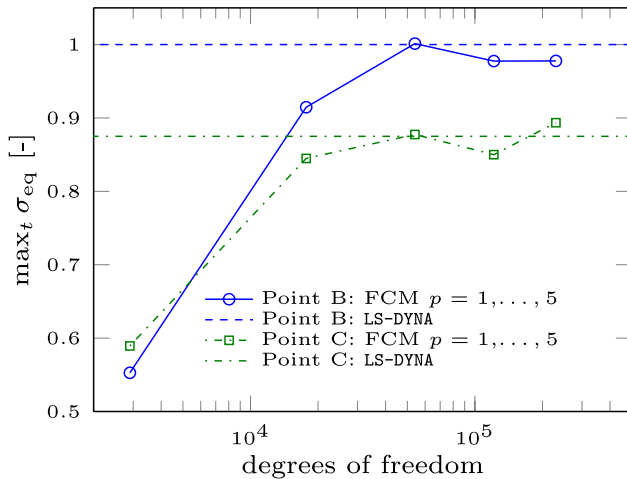
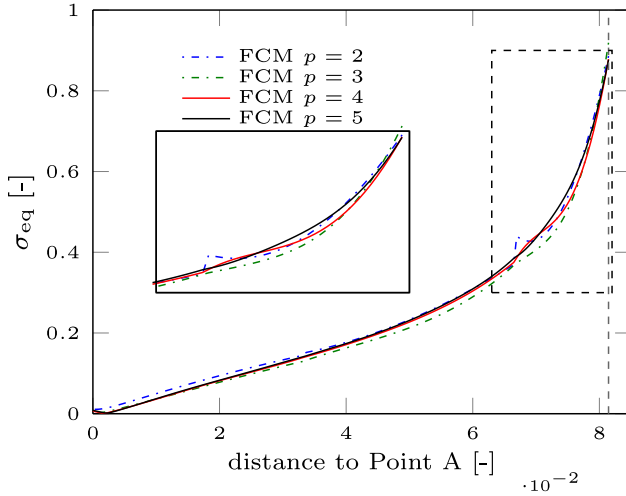
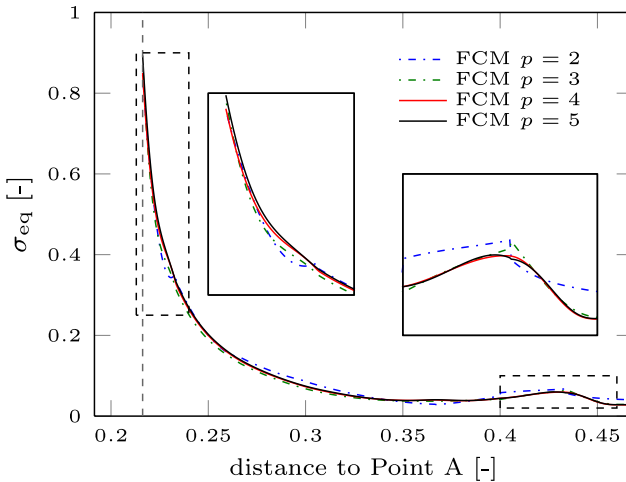


Fig. 29. Convergence of maximum von Mises stress at Point B.



(a)



(b)

Fig. 30. Von Mises peak stress distribution. (a) von Mises stress along line AB. (b) von Mises stress along line CE.

values for the energy. It can be observed that these results are closest to the numerical solution obtained with FCM using $p = 3$, for both pointwise and global values. By using a nonconforming high order discretization, the same level of accuracy is obtained with FCM using significantly fewer degrees of freedom.

Difficulties in the pointwise convergence of the computed stresses in the vicinity of the slotted hole are experienced for uniform p -extension. Local refinement of the finite element mesh around the hole is necessary to obtain an accurate solution.

3.2.4. Notes on computational performance

For practical significance, we should also consider the computational performance of the FCM, in terms of hardware requirements and computation time.

The numerical integration of the stiffness and mass matrices constitute most of the total computational time for the p -version of the FCM.²⁴ For 3D problems, the total number of floating point operations required for a straight-forward numerical integration is of order $\mathcal{O}(p^9)$. This cost is even much more predominant in the context of the FCM, as the adaptive integration scheme results in a very large number of integration points. Fortunately, this problem is well suited for parallelization, as there is no dependency between the integration points. Major performance gain is achieved in **AdhoC++** utilizing shared memory parallelization of the integration loop using OpenMP.

For implicit transient analysis, a system of linear equations needs to be solved at each time step. Hence, a fast, robust linear solver is an essential component for transient FCM analysis. Since the system matrices of the FCM are rather ill-conditioned due to penalization of fictitious domain, iterative solvers practically cannot be used. This renders using a direct sparse solver a more feasible option.

AdhoC++ interfaces with **UMFPACK**,²⁵ which is a fast and robust sparse direct solver. **UMFPACK** performs a sparse LU factorization using an unsymmetric pattern multi-frontal method. The result is then obtained using forward and backward solution of the factorized system.²⁶ As most of the solution effort is spent on the sparse LU factorization, the factorized matrices are cached and only the forward and backward solution are performed at each time step.

The total computational time and main memory requirements for the FCM computation are shown in Table 1. All FCM computations were performed on two eight core Intel[®]Xeon[®]E5-2690 CPUs @ 2.9 GHz, with 20 MB L2 cache, and 192 GB of main memory. Note, however, that **UMFPACK** is a serial solver. Here it is important to point out that the implicit FCM analysis achieves the same range of accuracy as the explicit **LS-DYNA** analysis with $p = 3$ and 54,021 degrees of freedom for the quarter model.

Even more important than computational time is the engineering time required to set up a computational model on the basis of a CAD drawing. Note that the adaptive integration sub-cell grid which is used by the FCM analysis is obtained

Table 1. Computational performance with **AdhoC++**.

p	N	Total memory (MB)	Integration time	Solution time	Total time
1	2,901	170	2 m 12 s	2 s	2 m 47 s
2	17,709	534	4 m 01 s	52 s	5 m 39 s
3	54,021	2,264	9 m 09 s	5 m 06 s	15 m 33 s
4	121,431	8,830	25 m 30 s	13 m 56 s	46 m 27 s
5	229,533	24,422	2 h 26 m 07 s	56 m 10 s	3 h 26 m 24 s

automatically, whereas the human labor for setting up an analysis-suitable finite element mesh exceeds by far the computational time for analysis.

4. Conclusions and Outlook

In the present contribution, the finite cell method was applied to solve transient problems of linear elastodynamics. The mathematical formulation was presented, following from the weak form of the initial/boundary value problem. A simple 1D benchmark problem was solved using FCM, illustrating the basic properties of the numerical solution. Finally, an example of transient problems from an industrial application was solved using FCM, where the results were in good accordance with the numerical solution obtained using state-of-the-art commercial software.

The results presented herein demonstrate the capability of FCM for solving transient problems of linear elastodynamics. Firstly, the spatial discretization using the FCM avoids the geometric complexity on the mesh level by considering a simpler shaped domain for discretization. The CAD model is used directly to describe the geometry in the framework of FCM, thereby circumventing the need to generate a mesh suitable for finite element analysis. Furthermore, FCM benefits from its high order p -version approximation basis, having higher convergence rates, and locking-free behavior. Consequently, a system with a relatively small number of degrees of freedom is generated, making implicit time integration a feasible choice.

These results offer several interesting options for future development:

- The application of hierarchical hp - d adaptivity, which is a suitable method for local mesh refinement in the framework of FCM would be highly interesting. For problems with nonsmooth and irregular solutions, local refinement can reduce computational effort in terms of degrees of freedom considerably.²⁰ The impact on the computational efficiency would be even more pronounced for transient analysis with implicit time integration.
- Using B-splines as an approximation basis for spatial discretization provides an attractive alternative in the context of isogeometric analysis and the finite cell method.¹⁰ It was shown that B-splines yield superior discrete spectra in comparison with p -version basis functions.⁴ Particularly, the higher modes converge better with increasing polynomial degrees when compared to the p -version. This would be advantageous when solving problems predominantly involving higher modes in the solution (e.g. wave propagation).
- The numerical integration cost for FCM could be significantly reduced by the reduction of the number of cut cells. The use of a rotationally symmetric embedding domain would be highly advantageous for problems dealing with shafts and cylindrical components. This approach would significantly reduce the integration cost, while maintaining the advantage of FCM regarding meshing, as only the cross section needs to be meshed in a 2D plane.

References

1. R. Norton, *Machine Design: An Integrated Approach, 2/E* (Pearson Education, New Jersey, 2000).
2. K. J. Bathe, *Finite Element Procedures* (Prentice Hall, New Jersey, 2007).
3. T. J. R. Hughes, *The Finite Element Method: Linear Static and Dynamic Finite Element Analysis* (Dover Publications, Mineola, NY, 2000).
4. J. Cottrell, T. J. Hughes and Y. Bazilevs, *Isogeometric Analysis: Toward Integration of CAD and FEA* (Wiley and Sons, New York, 2009).
5. Livermore Software Technology Corporation, LS-Dyna 971 R5 users manual.
6. J. Parvzian, A. Düster and E. Rank, Finite cell method, *Comput. Mech.* **41** (2007) 121–133.
7. A. Düster, J. Parvzian, Z. Yang and E. Rank, The finite cell method for three-dimensional problems of solid mechanics, *Comput. Meth. Appl. Mech. Eng.* **197** (2008) 3768–3782.
8. D. Schillinger, A. Düster and E. Rank, The hp-d-adaptive finite cell method for geometrically nonlinear problems of solid mechanics, *Int. J. Numer. Meth. Eng.* **89**(9) (2012) 1171–1202.
9. D. Schillinger, L. Dedé, M. A. Scott, J. A. Evans, M. J. Borden, E. Rank and T. J. Hughes, An isogeometric design-through-analysis methodology based on adaptive hierarchical refinement of NURBS, immersed boundary methods, and t-spline CAD surfaces, *Comput. Meth. Appl. Mech. Eng.* **249–252** (2012) 116–150.
10. D. Schillinger, M. Ruess, N. Zander, Y. Bazilevs, A. Düster and E. Rank, Small and large deformation analysis with the p- and b-spline versions of the finite cell method, *Comput. Mech.* **50** (2012) 445–478.
11. A. Abedian, J. Parvzian, A. Düster and E. Rank, Finite cell method compared to h-version finite element method for elasto-plastic problems, *Appl. Math. Mech.-Engl. Ed.* **35** (2014) 1239–1248.
12. E. Rank, S. Kollmannsberger, C. Sorger and A. Düster, Shell finite cell method: A high order fictitious domain approach for thin-walled structures, *Comput. Meth. Appl. Mech. Eng.* **200** (2011) 3200–3209.
13. M. Ruess, D. Tal, N. Trabelsi, Z. Yosibash and E. Rank, The finite cell method for bone simulations: Verification and validation, *Biomech. Model. Mechanobiol.* **11** (2012) 425–437.
14. M. Joulaian and A. Düster, Local enrichment of the finite cell method for problems with material interfaces, *Comput. Mech.* **52** (2013) 741–762.
15. N. Zander, T. Bog, S. Kollmannsberger, D. Schillinger and E. Rank, Multi-level hp-adaptivity: High-order mesh adaptivity without the difficulties of constraining hanging nodes, *Comput. Mech.* (2015), accepted for publication.
16. M. Joulaian, S. Duczek, U. Gabbert and A. Düster, Finite and spectral cell method for wave propagation in heterogeneous materials, *Comput. Mech.* **54**(3) (2014) 661–675.
17. B. Reddy, *Introductory Functional Analysis: With Applications to Boundary Value Problems and Finite Elements*, Introductory Functional Analysis Series (U.S. Government Printing Office, New York, 1998).
18. A. Abedian, J. Parvzian, A. Düster, H. Khademyzadeh and E. Rank, Performance of different integration schemes in facing discontinuities in the finite cell method, *Int. J. Comput. Meth.* **10** (2013) 1350002.
19. S. Rao, *Mechanical Vibrations* (Addison-Wesley Longman, Incorporated, 1986).
20. B. A. Szabó, *Finite Element Analysis* (John Wiley & Sons, New York, 1991).
21. S. Bindick, M. Stiebler and M. Krafczyk, Fast kd-tree-based hierarchical radiosity for radiative heat transport problems, *Int. J. Numer. Meth. Eng.* **86**(9) (2011) 1082–1100.

22. R. McNeel, Rhinoceros 3D, March 2014.
23. A. Düster, H. Bröker and E. Rank, The p-version of the finite element method for three-dimensional curved thin walled structures, *Int. J. Numer. Meth. Eng.* **52**(7) (2001) 673–703.
24. J. M. Melenk, K. Gerdes and C. Schwab, Fully discrete *hp*-finite elements: Fast quadrature, tech. rep., ETH Zürich, September 1999.
25. T. Davis and I. Duff, An unsymmetric-pattern multifrontal method for sparse LU factorization, *SIAM J. Matrix Anal. Appl.* **18** (1997) 140–158.
26. E. Kreyszig, H. Kreyszig and E. J. Norminton, *Adv. Eng. Math.*, 10th edn. (Wiley, Hoboken, N.J., 2011).